RSC Advances

PAPER

View Article Online
View Journal | View Issue

Cite this: *RSC Adv.*, 2026, **16**, 25011

Anti-obesity effects of secondary metabolites from *Chrysosplenium flagelliferum*: *in vitro* and *in silico* studies

Eun Jin Heo,†[ab] Bowon Jung,†[ab] Sunbeom Kwon,[ab] Min Yeong Choi,[c] Yoon Seo Jang,[d] Ki Hyun Kim,[d] Gwang Hun Park,[c] Ji Ah Kim*[c] and Seulah Lee*[ab]

Received 29th January 2026
Accepted 4th May 2026

DOI: 10.1039/d6ra00782a

rsc.li/rsc-advances

From the extract of *Chrysosplenium flagelliferum*, a Korean forest medicinal plant, a new triterpene glycoside (**1**), four triterpenoids (**2–5**), four flavonoids (**6–9**), a monoterpene lactone (**10**), a phenolic compound (**11**) and an alkaloid (**12**) were isolated. All isolates were evaluated for their anti-obesity effects, where cucurbitacin D (**2**) and cirsimaritin (**6**) exhibited significant inhibitory activities against lipid accumulation in differentiating 3T3-L1 adipocytes and downregulated the expression of PPAR-γ. Based on this, both compounds were subjected to molecular docking and dynamics simulation with PPAR-γ. Compound **2** showed dynamic binding behavior driven by conformational flexibility, while compound **6** maintained a stable and compact binding pose, suggesting they engage PPAR-γ through distinct binding modes and differential molecular mechanisms. In conclusion, this study suggests that *C. flagelliferum* is a promising source of anti-obesity agents and provides insight into molecular mechanisms of its bioactive compounds, highlighting their potential as therapeutic candidates for metabolic disorders.

1 Introduction

Chrysosplenium L. belongs to the family Saxifragaceae.[1] It comprises approximately 70 species and is predominantly distributed in the Northern Hemisphere.[2,3] In Korea, various species are predominantly native, including *C. flagelliferum* F. Shmidt, *C. alternifolium* var.*sibiricum* Seringe ex DC., *C. japonicum* (Maxim.) Makino, *C. ramosum* Maxim., *C. pseudofauriei* H. Lév., *C. flaviflorum* Ohwi, *C. pilosum* var.*fulvum* (Terracc.) Hara, and *C. pilosum* var. *valdepilosum* Ohwi.[4] These species exhibit variations in chemical composition that are suggested to be associated with differences in habit conditions.[5] Phytochemical studies of the genus *Chrysosplenium* have revealed that the genus contains highly hydroxylated and methoxylated flavonoids and triterpenoids as its bioactive compounds.[6–8] These compounds have demonstrated various bioactivities, including antimicrobial,[9] cytotoxic,[10–12] and antiviral effect.[13] Of particular interest, *O*-methylated flavonoids predominantly isolated from the genus *Chrysosplenium* have been reported to exert anti-obesity effects by promoting lipid breakdown and upregulating the expression of lipolysis-related genes.[6,14] Despite their biological potential, studies on the metabolite composition of the Korean native species *C. flagelliferum* are limited, and the biological activities of its constituent compounds remain largely unexplored.

Obesity is defined as an excess of fatty tissue in the body, which increases the risk of a variety of chronic illnesses and body function disorders.[15] According to the World Health Organization (WHO), 2.5 billion adults aged 18 years and older were overweight in 2022. By 2024, an estimated 35 million children under the age of 5 years were overweight. Alarmingly, the prevalence of obesity is shifting toward younger age groups, accompanied by a rising number of deaths from obesity-associated comorbidities. Furthermore, obesity is closely related to metabolic disorders including inflammation, type 2 diabetes, and non-alcoholic fatty liver disease (NAFLD).[16] These metabolic disorders are caused by an imbalance in glucose and lipid metabolism in adipose tissue and liver. Therefore, the regulation of size and number of adipocytes is important for anti-obesity therapy. Adipogenesis, a differentiation process of precursor cells into mature adipocytes,[17] is tightly regulated by transcription factors such as CCAAT/enhancer-binding proteins (C/EBPs), peroxisome proliferator-activated receptor-γ (PPAR-γ), and sterol regulatory element binding protein (SREBP). While previous studies have reported anti-obesity effects of *C. flagelliferum* extracts,[18] specific bioactive compounds responsible for these effects have remained unstudied.

[a]*Department of Convergent Biotechnology and Advanced Materials Science, BK21 Interdisciplinary Program in IT-Bio Convergence System, Kyung Hee University, Yongin 17104, Republic of Korea. E-mail: lee.seulah@khu.ac.kr*

[b]*Center for Space Biomedical Sciences, G-LAMP NEXUS Institute, Kyung Hee University, Yongin 17104, Republic of Korea*

[c]*Forest Medicinal Resources Research Center, National Institute of Forest Science, Yeongju 36040, Republic of Korea. E-mail: jiahkim@korea.kr*

[d]*School of Pharmacy, Sungkyunkwan University, Suwon 16419, Republic of Korea*

† These authors contributed equally to this work.

As part of our endeavor searching for bioactive natural products from Korean forest medicinal plants, we performed chemical analysis on the ethanolic extract of *C. flagelliferum*. After repetitive chromatographic methods, a new triterpene glycoside (**1**), four triterpenoids (**2–5**), four flavonoids (**6–9**), a monoterpene lactone (**10**), a phenolic compound (**11**) and an alkaloid (**12**) were identified and evaluated for their anti-obesity effects, followed by *in silico* molecular docking and dynamic simulation with PPAR-γ.

2 Materials and methods

2.1. General experimental procedures

NMR spectra were measured using a Bruker AVANCE III operating at 600 MHz (^{1}H) and 150 MHz (^{13}C) (Bruker, MA, USA). LC/MS analysis was performed using ACQUITY UPLC H-Class System with SQ detector. Preparative high-performance liquid chromatography (HPLC) was conducted using semi-preparative HPLC was conducted on Waters 1525 binary HPLC pump equipped with Waters 996 photodiode array detector (Waters, MA, USA). Luna® C18 (5 μm, 250 × 10 mm, 2.0 mL min^{-1}) (Phenomenex) and Luna® Phenyl-Hexyl (10 μm, 250 × 10 mm, 2.0 mL min^{-1}) (Phenomenex) columns were used. Column chromatography was performed using silica gel (SKY SIL, SL-60-60A, 70–230 mesh, SK chemical, South Korea) and C_{18}-reversed phase silica gel (550–950 mesh, Supelco, Germany). Waters Sep-Pak® C18 20cc Vac Cartridge and Silica 20cc Vac Cartridge. Thin-layer chromatography (TLC) was conducted using aluminum foil- or glass-backed silica gel 60 F_{254} plates and reverse-phase (RP)-18 F_{254s} plates (Merck). Spots on TLC were detected using UV and heating after dipping in anisaldehyde.

2.2. Sample material

Chrysosplenium flagelliferum was collected from Bonghwa, Yeongyang, and Taebaek, Korea. A voucher specimen (FMRC_230403) was authenticated by Dr Yong-Hwan Son and was deposited at the Forest Medicinal Resources Research Center, National Institute of Forest Science, Korea.

2.3. Molecular networking

The molecular networks were generated by aligning each MS² fragmentation spectrum using GNPS, a web-based platform (https://gnps.ucsd.edu/ProteoSAFe/static/gnps-splash.jsp).[19] Initially, MS2 spectra data were acquired using an Agilent 1290 Infinity II HPLC system (Agilent Technologies, Santa Clara, CA, USA) coupled with an Agilent G6548B quadrupole time-of-flight (Q-Tof) mass spectrometer (Agilent Technologies, Santa Clara, CA, USA). A Dual AJS ESI ion source was utilized. The Agilent G6548B Q-TOF Mass Spectrometer was further equipped with a G7104A quaternary pump, G7116B autosampler, and G7117B diode array detector (DAD). Chromatographic separation was performed on an Acquity® UPLC BEH reverse-phase column C18 (150 mm × 2.1 mm, 1.7 μM). The mobile phase consisted of 0.1% formic acid in H_2O (A) and acetonitrile (B), with a gradient elution as follows: 0–1 min, 10% (B); 1–16 min, 10–100% (B); 16–18 min, 100% (B). The flow rate was maintained at 0.4 mL min^{-1}. MS/MS analysis was conducted using electrospray ionization (ESI) in positive ion mode, with an *m*/*z* range of 50–1000 and a collision energy of 30 eV. The voltages were set as follows: capillary, 3500 V; nozzle, 1000 V; fragmentor, 100 V; and skimmer, 65 V. The source gas temperature was maintained at 320 °C, with a gas flow rate of 8 L min^{-1}, and nebulizer pressure of 40 psig. Additionally, the raw MS² data should be converted to mzML, mzXML or MGF file format using MSConvert tool of ProteoWizard MSConvert version 3 software. The processed MS² data were then uploaded to the GNPS platform *via* WinSCP, following the Classical Molecular Networking workflow. The molecular networking parameters were set as follows: Precursor Ion Mass Tolerance and Fragment Ion Mass Tolerance were both set be 0.02 Da, the Minimum Pairs Cosine Score was set to 0.5, the Minimum Number of Common Fragment Ions shared between two consensus MS/MS spectra was set to 3, and minimum number of MS/MS spectra required in a consensus MS/MS spectra was set to 1.

2.4. Extraction and isolation

The whole parts of *C. flagelliferum* (1.5 kg) were ground and extracted by maceration in 70% ethanol (EtOH) (v/v in water) at room temperature for 24 hours. After filtration, the solvent was evaporated under reduced pressure to yield an EtOH extract (392.0 g). The extract was suspended in distilled water and sequentially partitioned based on polarity using hexane, dichloromethane (CH_2Cl_2), ethyl acetate (EtOAc), and *n*-BuOH. The CH_2Cl_2 layer (26.0 g) was subjected to silica gel column chromatography (CC) and eluted with a gradient solvent system of CH_2Cl_2 : MeOH (40 : 1 to 5 : 1) to yield five fractions (CFM1–CFM5). Fraction CFM5 (888.3 mg) was subjected to Sep-pak® C18 20cc vac cartridge and eluted with MeOH : H_2O (5 : 5 to 0 : 10), resulting in three subfractions (CFM51–CFM53). Subfraction CFM51 (13.7 mg) was separated using HPLC (Luna® C18, 5 μm, 250 × 10 mm, 2.0 mL min^{-1}) with the solvent system of MeOH : H_2O (43 : 57), to give compound **1** (61.0 min, 0.9 mg). The EtOAc layer (33.0 g) was applied to silica gel CC and eluted with a gradient solvent system of CH_2Cl_2 : MeOH (20 : 1 to 5 : 1) to yield ten fractions (CFE1–CFE10). Fraction CFE3 (211.0 mg) was subjected to Sep-pak® C18 20cc vac cartridge and eluted with MeOH : H_2O (7 : 3 to 0 : 10) as the solvent system, resulting in six subfractions (CFE31–CFE36). Subfractions CFE32 and CFE33 were combined based on their similar TLC spots, and the combined fraction (25.0 mg) was purified using HPLC (Luna® C18, 5 μm, 250 × 10 mm, 2.0 mL min^{-1}) with the solvent system of MeOH : H_2O (40 : 60), to yield compounds **10** (18.2 min, 0.8 mg) and **11** (29.2 min, 0.2 mg). Meanwhile, the combined fraction of CFE34 and CFE35 (44.0 mg) was purified by HPLC (Luna® C18, 5 μm, 250 × 10 mm, 2.0 mL min^{-1}) with the solvent system of MeOH : H_2O (65 : 35) to give **2** (21.4 min, 0.5 mg), **6** (27.7 min, 1.5 mg), **7** (31.7 min, 2.8 mg), and **8** (12.3 min, 4.2 mg). Fraction CFE5 (205.0 mg) was applied to Sep-pak® C18 20cc vac cartridge and eluted with a gradient solvent system of MeOH : H_2O (7 : 3 to 0 : 10), yielding eight subfractions (CFE51–CFE58). Subfractions CFE52 and CFE53 were consolidated based on similar TLC spots, and the combined fraction (60.6

mg) was further purified using HPLC (Luna® Phenyl-hexyl, 10 μm, 250 × 10 mm, 2.0 mL min^{-1}) with the solvent system of MeOH : H_2O (40 : 60) to give compound **12** (7.8 min, 3.5 mg). Fraction CFE6 (400.0 mg) was purified using Sep-pak® C18 20cc vac cartridge with MeOH : H_2O (7 : 3 to 0 : 10) to give seven subfractions (CFE61–CFE67). Subfractions CFE64 and CFE65 were combined (127.1 mg), which was subjected to Sep-pak® silica 20cc vac cartridge with the gradient solvent system CH_2Cl_2 : MeOH (20 : 1 to 10 : 1), resulting in eight subfractions (CFE641–CFE648). CFE646 (70.7 mg) was further purified by HPLC (Luna® Phenyl-hexyl, 10 μm, 250 × 10 mm, 2.0 mL min^{-1}) with MeOH : H_2O (40 : 60), resulting in six subfractions (CFE6461–CFE6466). CFE6466 (19.9 mg) was further purified using HPLC (Luna® C18, 10 μm, 250 × 10 mm, 2.0 mL min^{-1}) eluted with MeOH : H_2O (65 : 35), to give compounds **3** (16.4 min, 0.7 mg) and **4** (24.7 min, 8.5 mg). Compound **5** (36.6 min, 3.1 mg) was isolated from CFE647 (20.7 mg) by using HPLC (Luna® Phenyl-hexyl, 10 μm, 250 × 10 mm, 2.0 mL min^{-1}) with the solvent system of MeOH : H_2O (65 : 35). Fraction CFE7 (2.1 g) was subjected to an ODS column chromatography and eluted with acetone : H_2O (1 : 3), which yielded seven subfractions (CFE71–CFE77). Subfraction CFE77 (46.8 mg) was further purified using Sep-pak® silica 20cc vac cartridge with the gradient solvent system of CH_2Cl_2 : MeOH (20 : 1 to 5 : 1), resulting in twelve subfractions (CFE771 to CFE7712). Subfraction CFE775, 776 and 777 were combined based on their similar TLC patterns, and the combined fraction (30.1 mg) was further purified using HPLC (Luna® C18, 5 μm, 250 × 10 mm, 2 mL min^{-1}) with the solvent system of MeOH : H_2O (53 : 47), to give compound **9** (25.6 min, 0.5 mg).

2.4.1. Flagenin (1). Yellow gum; $[\alpha]_D^{23}$ + 7.5° (c 0.04 MeOH); UV (MeOH) λ_{max} (log ε) 215 (4.12) nm; IR (ATR) ν_{max} 3315, 2942, 2830, 1449, 1114, 1021, 626 cm^{-1}; ECD (MeOH) λ_{max} ($\Delta\varepsilon$) 204 (+8.92), 297 (+2.50) nm; ^{1}H (850 MHz) and ^{13}C (212.5 MHz) NMR data, see Table 1; ESI-MS (negative-ion mode) *m*/*z* 711.7 [M + FA–H]$^-$; HR-ESI-MS (negative-ion mode) *m*/*z* 711.3970 [M + FA–H]$^-$ (calcd for $C_{37}H_{59}O_{13}$, 711.3979).

Table 1 ^{1}H NMR (850 MHz) and ^{13}C NMR data (212.5 MHz) of compound **1** (CD_3OD)

	1	
Position	δ_H	δ_C
1	1.36 d (13.19), 1.42 d (12.25)	28.43
2	3.80 m	67.86
3	3.26 d (1.96)	78.59
4		41.35
5		138.33
6	5.58 d (5.76)	119.80
7	1.86 dd (5.81, 19.16), 2.32 m	23.47
8	1.83 d (8.11)	43.19
9		48.54
10	2.39 d (12.18)	33.69
11		215.53
12	3.18, 2.37 m	48.58
13		50.66
14		48.16
15	1.38 m, 1.76 dd (8.73, 12.71)	45.02
16	4.48 m	71.82
17	2.48 d (6.83)	58.38
18	0.77 s	19.06
19	1.01 s	18.92
20		74.11
21	1.33 s	26.03
22	1.50 dd (2.28, 14.70), 2.07 dd (9.09, 14.85)	48.58
23	4.84 m	70.11
24	5.04 d (9.61)	125.11
25		135.90
26	1.65 s	24.48
27	1.63 s	17.04
28	0.95 s	26.18
29	1.09 s	24.75
30	1.22 s	18.31
1′	4.09 d (7.86)	98.86
2′	3.08 m	73.56
3′	3.19 m	76.78
4′	3.10 m	70.62
5′	3.07 m	76.86
6′	3.53 dd (5.95, 11.73), 3.78 dd (1.75, 11.83)	61.66

2.5. Computational analysis

Conformer searches were conducted in MacroModel (Schrödinger Release 2025-3: MacroModel, Schrödinger, LLC, New York, NY, 2025) employing the mixed torsional/low mode sampling method with the MMFF force field. The searches were carried out in the gas phase with an energy window of 20 kJ mol^{-1}, and up to 10 000 steps were used to explore the potential conformers. The generated conformers were then subjected to energy minimization using the Polak–Ribiere conjugate gradient (PRCG) algorithm, with a maximum of 10 000 iterations and an RMS gradient convergence criterion of 0.001 kJ $(mol\ Å)^{-1}$. Conformers within 10 kJ mol^{-1} of the MMFF global minimum were selected and subsequently optimized in Tmolex 2025 (BIOVIA) at the DFT settings (B3LYP/M3 grid size), geometry optimization settings (energy 10^{-6} hartree, gradient norm $|dE/dxyz| = 10^{-3}$ hartree $bohr^{-1}$), and the basis set 6-31G(d,p) for all atoms.[20–22]

Based on the optimized geometries, ECD spectra were calculated at same theory level and basis set. The obtained CD spectra of **1a** and **1b** were generated by overlaying each transition according to the following equation:

$$\Delta\varepsilon(E) = \frac{1}{2.297 \times 10^{-39}} \frac{1}{\sqrt{2\pi}\sigma} \sum_{i}^{A} \Delta E_i R_i \, e^{[-(E-\Delta E_i/2\sigma)]^2}$$

where σ is the bandwidth at height $1/e$ and ΔE_i and R_i are the excitation energy and rotatory strength for transition i, respectively. In this study, the value of σ was 0.1 eV. ECD spectra were visualized using GraphPad Prism 10.

NMR shielding constants were then calculated for the optimized ground-state geometries at the B3LYP/6-31G(d,p) level. The ^{1}H and ^{13}C NMR chemical shifts of each isomer were obtained by Boltzmann averaging the calculated shielding values of the stable conformers at 298.15 K. Chemical shift values were obtained using the equation below:

$$\delta_{\mathrm{calc}}{}^{x} = \frac{\sigma^{\circ} - \sigma^{x}}{1 - \sigma^{\circ}/10^{6}}$$

where $\delta_{\mathrm{calc}}{}^{x}$ represents the calculated NMR chemical shift for nucleus x, and σ° corresponds to the shielding tensor of proton and carbon nuclei in tetramethylsilane, computed at the same level of theory.[23]

The DP4+ probability analysis was facilitated using an Excel sheet (DP4+) provided was evaluated against Grimblat *et al.*[24]

2.6. Enzymatic hydrolysis and sugar identification of 1

To elucidate the absolute configuration of the sugar moiety in compound **1**, 0.4 mg of compound **1** was hydrolyzed using β-glucosidase (1.0 mg, Sigma-Aldrich, St. Louis, MO, USA) from almonds, dissolved in 0.05 M sodium acetate buffer. The hydrolysis reaction was performed at 37 °C for 72 h in a dry oven. Upon cooling, the aglycone was extracted through solvent partitioning using ethyl acetate (EtOAc). The aqueous layer was then evaporated under vacuum, redissolved in 0.5 mL of anhydrous pyridine, and treated with 1 mg of L-cysteine methyl ester chloride. The mixture was heated at 60 °C for 1 h, followed by the addition of 50 μL of *O*-tolylisothiocyanate, and heated for another hour at the same temperature. The reaction mixture was concentrated, redissolved in methanol, and analyzed by analytical HPLC on ZORBAX SB-C8 column, using distilled water and acetonitrile as mobile phase. For comparison, standard substances of D-glucose and L-glucose underwent the same derivatization process and analyzed under identical conditions. Based on the HPLC analysis, the sugar moiety showed a retention time of 12.01 min, which was identical to that of D-glucose.

2.7. Cell culture and differentiation

3T3-L1 murine preadipocytes (American Type Culture Collection, Manassas, VA, USA) were cultured in DMEM/F-12 medium supplemented with 10% bovine calf serum (Gibco Inc. Grand Island), 100 U per mL penicillin (NY), and 100 μg per mL streptomycin (USA) in a CO_2 incubator at 37 °C with 5% CO_2. After two days of confluence, differentiation and lipid accumulation in 3T3-L1 cells were induced by treating the cells with DMI medium supplemented with 10% fetal bovine serum (FBS), 1 μM dexamethasone, 0.5 mM 3-isobutyl-1-methylxanthine (IBMX), and 10 μg mL^{-1} insulin for 48 hours. Thereafter, the medium was replaced with DMEM/F-12 containing 10% FBS. During this period, the 3T3-L1 cells were treated with compounds **1–12** with 20 μM.

2.8. *In vitro* cell viability assay

The cytotoxic effects of compounds **2** and **6** on 3T3-L1 preadipocytes were evaluated using a Cell Counting Kit-8 (CCK-8; Dojindo Laboratories, Kumamoto, Japan). Briefly, 3T3-L1 preadipocytes were seeded at a density of 5×10^4 cells per well in 96-well plates and incubated for 24 h. The cells were then treated with samples until day 4 of differentiation. After treatment, the medium was replaced with fresh medium containing 10 μL of CCK-8 solution, and the cells were incubated for 20 min. Absorbance was measured at 450 nm using a microplate reader. Cell viability was expressed as a percentage of the untreated control, which was set to 100%, and calculated using the following equation:

$$\text{Cell viability}(\%) = \frac{\text{OD sample}}{\text{mean OD control}} \times 100$$

2.9. Oil red O staining

Oil Red O staining was conducted to visually evaluate the effects of compounds **2** and **6** on lipid accumulation in 3T3-L1 cells. On day 8 post-induction, the differentiated 3T3-L1 cells were collected, rinsed twice with 1× Phosphate Buffered Saline (PBS), and subsequently fixed in 10% formalin at room temperature for at least 1 hour. The cells were then washed twice with distilled water and counterstained with 60% isopropanol for 5 min. Following a 5-minute incubation, the 3T3-L1 cells were thoroughly air-dried and subsequently stained with Oil Red O solution (60% isopropanol and 40% distilled water; Sigma-Aldrich St. Louis, MO, USA) for 20 minutes at room temperature. To quantify lipid accumulation, the cells were washed four times with distilled water, and the lipid droplets were observed using a optical microscope (Leica DMi8, Leica Microsystems GmbH, Wetzlar, Germany). Oil Red O dye was eluted with 100% isopropanol, and its absorbance was measured at 500 nm using a UV/Vis spectrophotometer (PerkinElmer, Waltham, MA, USA).

2.10. SDS-PAGE and western blot analysis

Cells treated with compounds **2** and **6** were washed with PBS and lysed in radio immunoprecipitation assay (RIPA) buffer (Cell Signaling, Beverly, MA, USA) supplemented with protease inhibitor cocktail and phosphatase inhibitor cocktail (Sigma-Aldrich). The lysates were centrifuged at 15 000 rpm for 10 min at 4 °C, and the supernatants were collected. Protein concentrations were determined using the BCA protein assay kit (Thermo Fisher Scientific; Waltham, MA USA) and separated by 10% SDS-polyacrylamide gel electrophoresis and transferred to polyvinylidene difluoride (PVDF) membranes (Bio-Rad, Herculues, CA, USA). The membranes were blocked with 5% skim milk for 30 min, followed by incubation with primary antibodies (CEBPα, PPAR-γ, Perilipin-1, FABP4, Bactin) diluted 1 : 500 for 18 hours. After incubation with secondary antibody in 5% nonfat milk in TBS-T at room temperature for 1 h, immunoreactive proteins were detected using a chemiluminescence ECL assay kit (Amersham Pharmacia Biosciences, England, UK) and visualized using a western blot scanner (Biorad, Chemidoc, MP imaging system, USA).

2.11. Molecular docking

Molecular docking calculations were conducted using Schrodinger docking suite (Schrödinger Maestro, Release 2024-4, Platform Windows-x64). Molecular docking studies of all isolated compounds were performed against PPAR-γ (PDB ID: 3E00). The protein X-ray crystal structure and 2D conformer of compounds were downloaded from Protein Data Bank (PDB, https://www.rcsb.org/) and PubChem database (https://

pubchem.ncbi.nlm.nih.gov/) respectively. The proteins and ligands were prepared and refined through energy minimization using the OPLS4 force field. This preparation ensured that they were in their lowest energy conformation. The grid sites were generated using the Glide Receptor Grid Generation tool, with a docking length of 20 Å. The grid centers were defined based on the centroid of the ligand within the workspace. Grids for each protein were individually designed based on the presence of the inhibitor. A grid was constructed with a focus on the inhibitor GW9662, centered within the binding site of the 3E00 protein structure. Ligand docking analyses were performed executing standard precision (SP) module. The ligand–protein interactions were demonstrated by Maestro interface. A lower docking score for the ligand–protein complex correlates with enhanced binding affinity. In this study, the binding energy calculations of optimized free proteins–ligand complex were performed with Molecular Mechanics-Generalized Born Surface Area (MM-GBSA). The MM-GBSA was calculated in the Prime module from Schrödinger suite using default settings, a more negative value indicates stronger binding.

2.12. Molecular dynamics

Molecular dynamic (MD) simulation is an *in silico* method employed to replicate and analyze interactions between a protein and ligand in a biological environment. To confirm the stability of the ligand–protein complex, an MD simulation was conducted for 200 ns on the complex with the highest binding affinity. For MD simulation studies, desmond integrated with Maestro was used. The ligand–protein complex was solvated by the TIP4P water molecules in orthorhombic box used (box distance (Å): a: 10.0, b: 10.0, c: 10.0; angles (°): α: 90.0, β: 90.0, γ: 90.0). The whole box was neutralized by adding sodium and chloride ions to the ligand–protein complexes. The force-field OPLS4 was employed to find the ligand–protein complex stability. After completing the MD simulation, various parameters, such as RMSD (root mean square deviation), RMSF (root mean square fluctuation) analysis were performed to evaluate the protein–ligand interactions.

2.13. Statistical analysis

All the data are shown as mean ± SD (standard deviation). Statistical significance was determined by Student's t-test. Differences with $^{*}P < 0.05$ and $^{*}P < 0.05$ were considered statistically significant.

3 Results and discussion

3.1. Isolation of compounds 1–12 from the extract of *C. flagelliferum*

Air-dried and powdered *C. flagelliferum* (1.5 kg) was extracted with 70% ethanol (EtOH), which provided the resultant EtOH extract. The extract was subjected to repetitive chromatographic techniques, resulting in the isolation of a new triterpene glycoside (**1**), four triterpenoids (**2–5**), four flavonoids (**6–9**), a monoterpene lactone (**10**), a phenolic compound (**11**) and an alkaloid (**12**) (Fig. 1). The isolated compounds were identified to be cucurbitacin D (**2**),[25] arvenin III (**3**),[26] arvenin I (**4**),[27] arvenin II

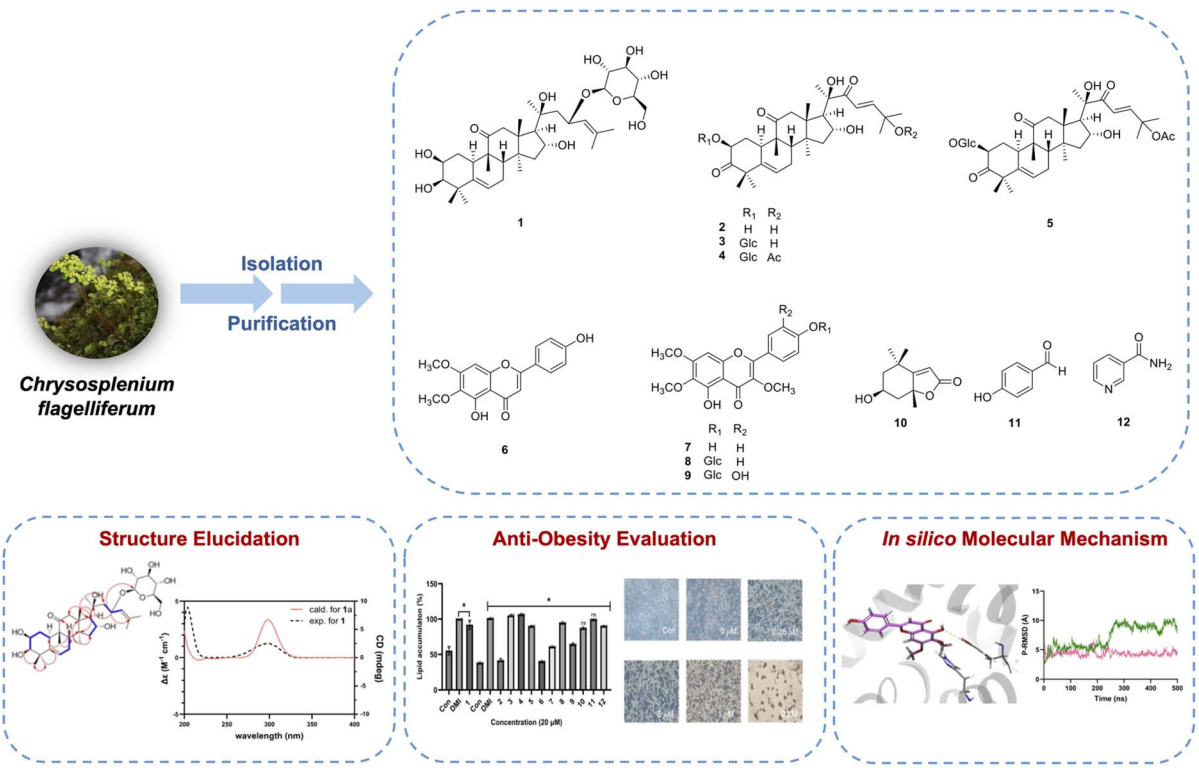

Fig. 1 Schematic representation of isolation of compounds **1–12** from *C. flagelliferum* (Glc; glucose).

(5),[28] cirsimaritin (6),[29] penduletin (7),[30] pendulin (8),[31] chrysosplenoside D (9),[32] loliolide (10),[10] 4-hydroxybenzaldehyde (11)[33] and nicotinamide (12),[34] by comparing their NMR spectroscopic and physical data with those previously reported.

3.2. Structural elucidation of flagenin (1)

Flagenin (1) was isolated as a yellow gum. The molecular formula was established as $C_{36}H_{58}O_{11}$, as confirmed by HRESIMS peak at m/z 711.3970 $[M + FA–H]^-$ obtained in negative-ion mode. The ^{1}H NMR data of **1** showed the presence of two olefinic hydrogens [δ_H 5.58 (1H, d, J = 5.8 Hz), 5.04 (1H, d, J = 9.6 Hz)], six methyl groups [δ_H 0.77 (3H, s), 0.95 (3H, s), 1.01 (3H, s), 1.09 (3H, s), 1.22 (3H, s), 1.33 (3H, s)], and two deshielded methyl groups [δ_H 1.63 (3H, s), 1.65 (3H, s)]. The anomeric proton of the sugar moiety was observed as a doublet at 4.09 ppm (J = 7.09 Hz), consistent with a β-anomeric configuration.[35] The ^{13}C NMR spectrum of **1** revealed a total of 36 carbon signals. These included a carbonyl carbon (δ_C 215.53), four olefinic carbons (δ_C 119.80, 125.90, 135.90, 138.33), and an anomeric carbon (δ_C 98.86). In addition, several oxygenated carbons were also observed, including those assigned to the sugar moiety (δ_C 70.62, 73.56, 76.86, 76.78, 61.66) and the remaining oxygenated carbons (δ_C 67.86, 70.11, 71.82, 78.59, 74.11). The NMR data of compound **1**, compared with those of cucurbitane-type terpenoid derivatives (**2–5**) identified in this study, suggested that compound **1** is a new cucurbitane-type terpenoid glycoside. The structure of compound **1** was further examined by 2D NMR experiments, including key HMBC and ^{1}H–^{1}H COSY (Fig. 2A). The HMBC correlations of H-3 (δ_H 3.26)/C-1 (δ_C 28.43), C-5 (δ_C 138.33), C-28 (δ_C 26.18), and C-29 (δ_C 24.75), H_3-28 (δ_H 0.95)/C-3 (δ_C 78.59), and H_3-29 (δ_H 1.09)/C-3 supported hydroxylation at C-3 on ring A. In addition, the ^{1}H–^{1}H COSY correlation of H-2 (δ_H 3.80)/H-3 established the vicinal relationship of two oxygenated methine protons on ring

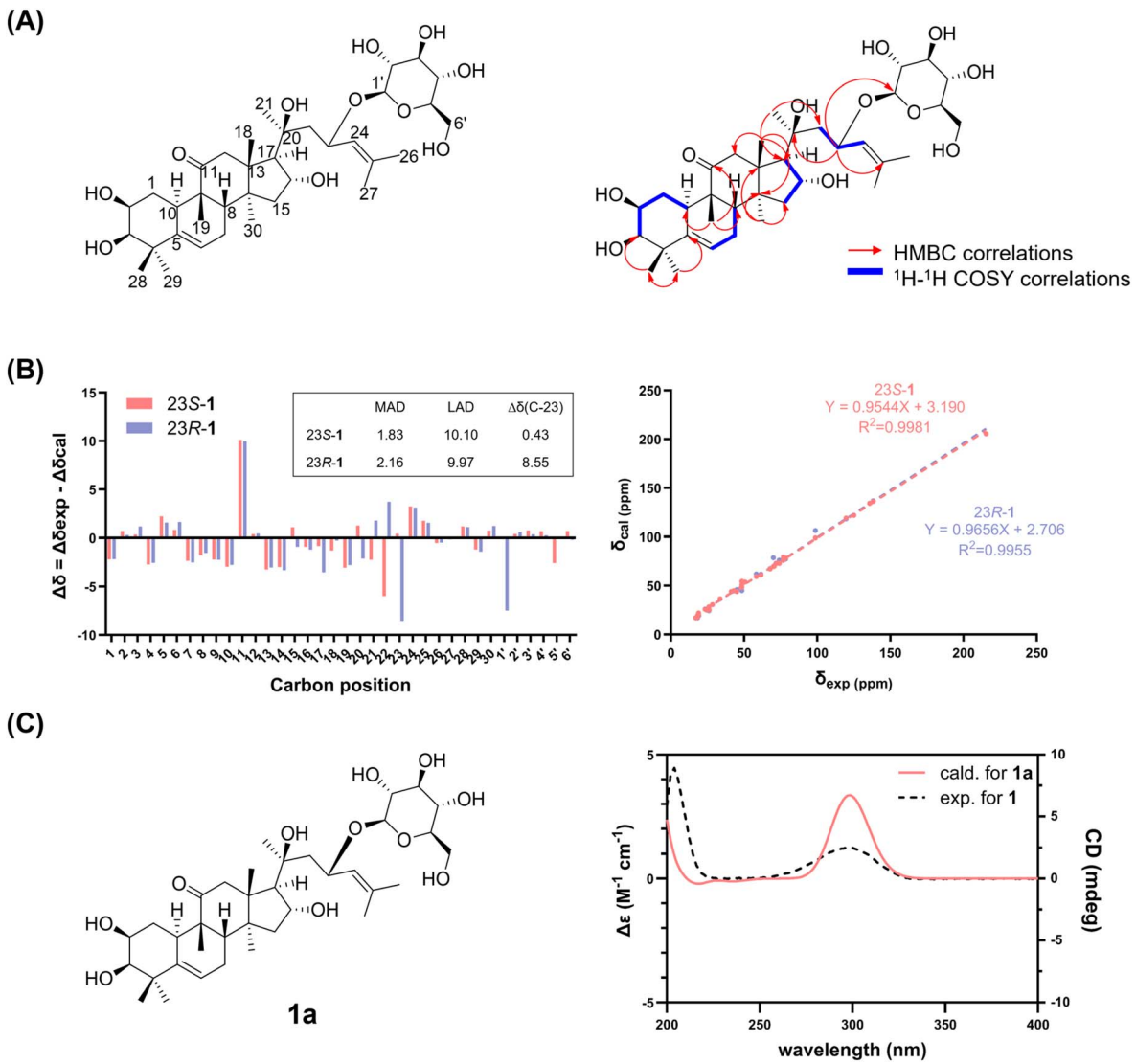

Fig. 2 (A) Key HMBC (arrows) and ^{1}H–^{1}H COSY (bold lines) correlations of compound **1**. (B) Relative errors and regression analysis of experimental *versus* calculated ^{13}C NMR chemical shifts for 23*S*-**1** and 23*R*-**1**. (C) Experimental and TD-DFT-calculated ECD spectra of **1**.

A, consistent with hydroxylation at C-2 and C-3. The coupling constant ($J = 2.0$ Hz) between H-2 and H-3 further indicated a *cis* relationship between these two hydroxyl groups.[36,37] Additionally, ROESY correlation between H-2 and H-10 (δ_H 2.39) suggested their spatial proximity, indicating that the hydroxyl groups at C-2 and C-3 are oriented on the face opposite to H-10. An olefinic bond at C-5/C-6 (δ_C 119.80) was assigned from the HMBC correlations of H_3-28 and H_3-29/C-5 and H_2-7 (δ_H 1.86, 2.37)/C-5 and C-6. The presence of a carbonyl group at C-11 on ring C was supported by the HMBC correlations of H-10, H_2-12 (δ_H 2.37, 3.18), and H_3-19 (δ_H 1.01)/C-11 (δ_C 215.53). Moreover, HMBC correlations of H_3-26 (δ_H 1.65) and H_3-27 (δ_H 1.63)/C-24 (δ_C 125.11) and C-25 (δ_C 135.90) were consistent with both methyl groups being attached to the olefinic carbon C-25. The presence of a glucose moiety at C-23 was confirmed based on HMBC correlations of H-23 (δ_H 4.84)/C′-1 and C-25, and H-1′ (δ_H 4.09)/C-23 (δ_C 70.11).

The stereochemistry of C-23 could not be definitively assigned, due to the free rotation of the side chain. The other stereochemical configurations of compound **1** are anticipated to be identical to those of cucurbitane-type terpenoids, indicating that the absolute configurations of **1** are 2*S*, 3*R*, 8*S*, 9*R*, 10*R*, 13*R*, 14*S*, 16*R*, 17*S*, and 20*S*. To provide further support for the assignment of the stereochemistry at C-23, quantum mechanical calculations of the NMR chemical shifts were carried out at the B3LYP/6-31G(d,p) level, considering the conformer of both the 23*S*-**1** and 23*R*-**1** isomers. The ^{1}H and ^{13}C NMR chemical shifts of 23*R*-**1** and 23*S*-**1** were computationally predicted and then compared with the experimental NMR data of compound **1** through DP4+ analysis, conclusively indicating that compound **1** corresponds to 23*S*-**1** with 100% probability. In addition, linear regression analysis of ^{13}C NMR chemical shifts gave the correlation coefficient (R^2) values of 0.9981 for 23*S*-**1** and 0.9955 for 23*R*-**1**. The values of mean absolute

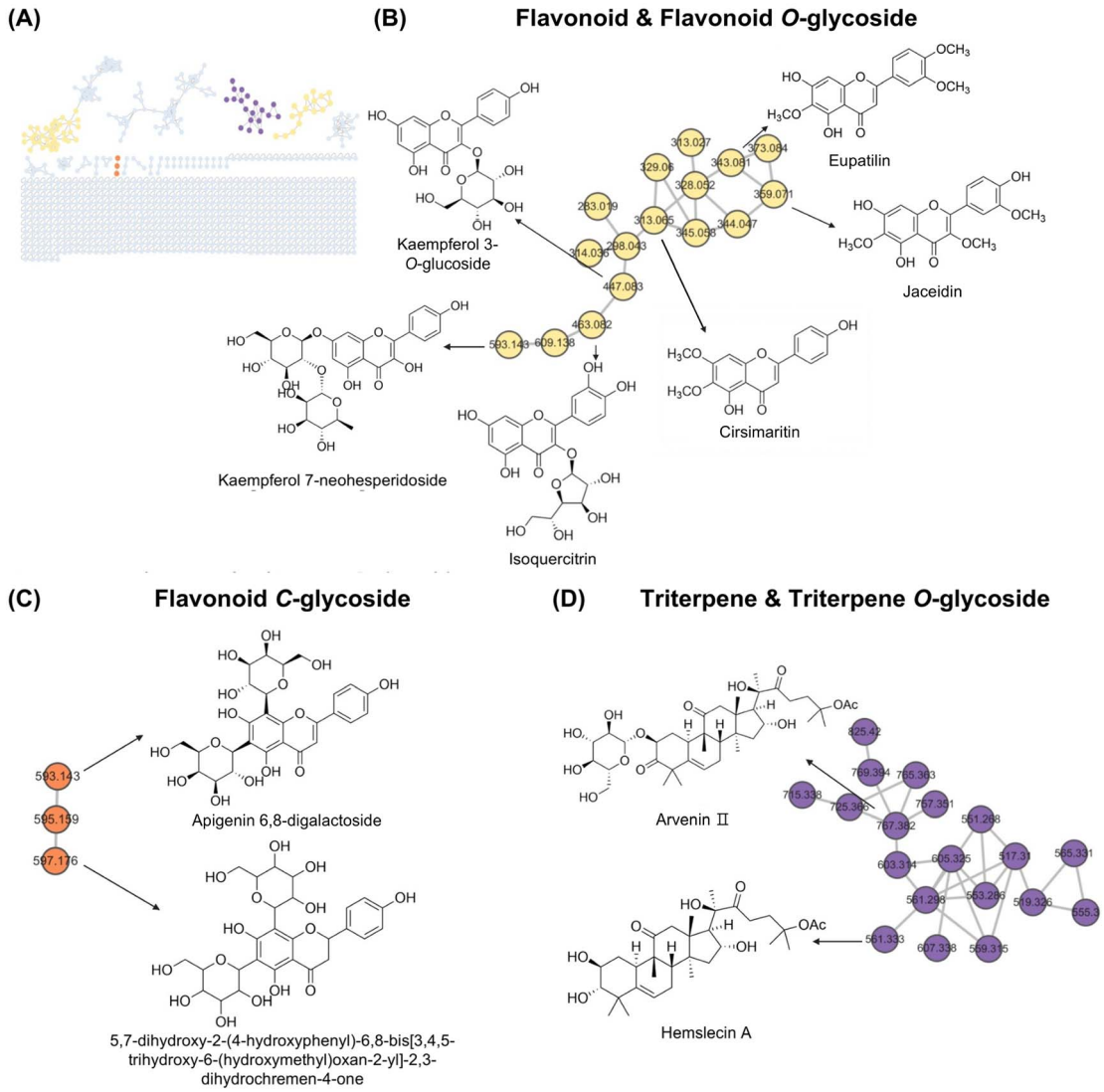

Fig. 3 (A) Molecular networks of the extract of *C. flagelliferum*, illustrating clusters based on MS/MS spectrum similarity. (B) Cluster of flavonoids and flavonoid *O*-glycosides. (C) Cluster of flavonoid *C*-glycosides. (D) Cluster of triterpenes and triterpene *O*-glycosides.

deviation (MAD) and largest absolute deviation (LAD) were 1.83 and 10.01 for 23*S*-**1** and 2.16 and 9.97 for 23*R*-**1**, respectively (Fig. 2B). Notably, the calculated ^{13}C NMR chemical shift of the stereogenic carbon C-23 was 69.68 ppm for 23*S*-1 and 78.66 ppm for 23*R*-1, whereas the experimental values was 70.11 ppm (Tables S1–3). The much closer agreement for 23*S*-1 further supports assignment of compound **1** as the 23*S* isomer.

To determine the absolute configuration of compound **1**, the experimental ECD spectrum was compared with TD-DFT-calculated spectra of the **1a** and **1b** enantiomers. The calculated ECD spectrum of **1a** closely matched the experimental spectrum, showing a positive Cotton effect at 297 nm (Fig. 2C). This structure represents a glycosylated terpene with a previously unreported carbon framework, which is clearly distinct from known cucurbitane-type terpenes. Accordingly, the complete structure of compound **1** was confirmed as named flagenin.

3.3. GNPS-based molecular networking

Each metabolite in the extract of *C. flagelliferum* was annotated through GNPS library based on the pairwise spectral similarity alignment. Nodes were clustered using the MS-Cluster algorithm, which groups compounds with the same core structure based on their similar MS/MS fragmentation patterns.[19,38] Molecular networking data from electrospray ionization mass spectrometry in negative ion mode revealed 824 nodes, which were categorized into 23 clusters and 671 single nodes (Fig. 3A). The cluster of flavonoids and flavonoid *O*-glycosides comprises nodes with *m*/*z* values of 313.065, 329.060, 343.081, 345.058, 359.071, 373.084, 447.083, 463.082, 593.143 and 609.138 (Fig. 3B). These were annotated as cirsimaritin, 4′,5,7-trihydroxy-3,6-dimethoxyflavone, eupatilin, viscidulin III, jaceidin, 5-hydroxy-2-(4-hydroxy-3-methoxyphenyl)-3,6,7-trimethoxy-4*H*-chromen-4-one, kaempferol-3-*O*-glucoside, isoquercitrin, kaempferol 7-neohesperidoside and quercetin-3-*O*-hexosyl-deoxyhexoside, respectively. The fragmentation pattern of cirsimaritin revealed peaks at *m*/*z* 163.0054 and 283.025, indicating a 30 Da neutral loss attributed to the cleavage of a methoxy group from the cirsimaritin molecule. Similarly, flavonoids such as eupatilin and viscidulin III, which contain methoxy groups, exhibited a neutral loss of 30 Da. Flavonoid *O*-glycosides such as isoquercitrin, quercetin 3-*O*-hexoxyl-deoxyhexoside, kaempferol 3-*O*-glucoside, and kaempferol 7-neohesperidoside exhibited fragmentation pattern peaks corresponding to their aglycone forms after the loss of their sugar moieties, with *m*/*z* values of 300.0290, 300.00284, 284.034 and 284.033, respectively. The cluster of flavonoid *C*-glycosides contained nodes at *m*/*z* 593.143 and 597.176, annotated as apigenin 6,8-digalactoside and 5,7-dihydroxy-2-(4-hydroxyphenyl)-6,8-bis[3,4,5-trihydroxy-6-(hydroxymethyl)oxan-2-yl]-2,3-dihydrochromen-4-one, respectively (Fig. 3C). The cluster of triterpenes and triterpene *O*-glycosides includes hemslecin A and arvenin II, with *m*/*z* values of 561.333 and 767.382, respectively (Fig. 3D). The molecular network revealed a high prevalence of flavonoids, triterpenes, and their respective glycosides, suggesting these metabolites are the primary constituents of the extract of *C. flagelliferum*, where arvenin II (**5**) and cirsimaritin (**6**) were isolated in the current study.

3.4. Inhibition of lipid accumulation in 3T3-L1 cells

The potential inhibitory effects of compounds **1–12** on lipid accumulation in differentiating 3T3-L1 adipocytes were

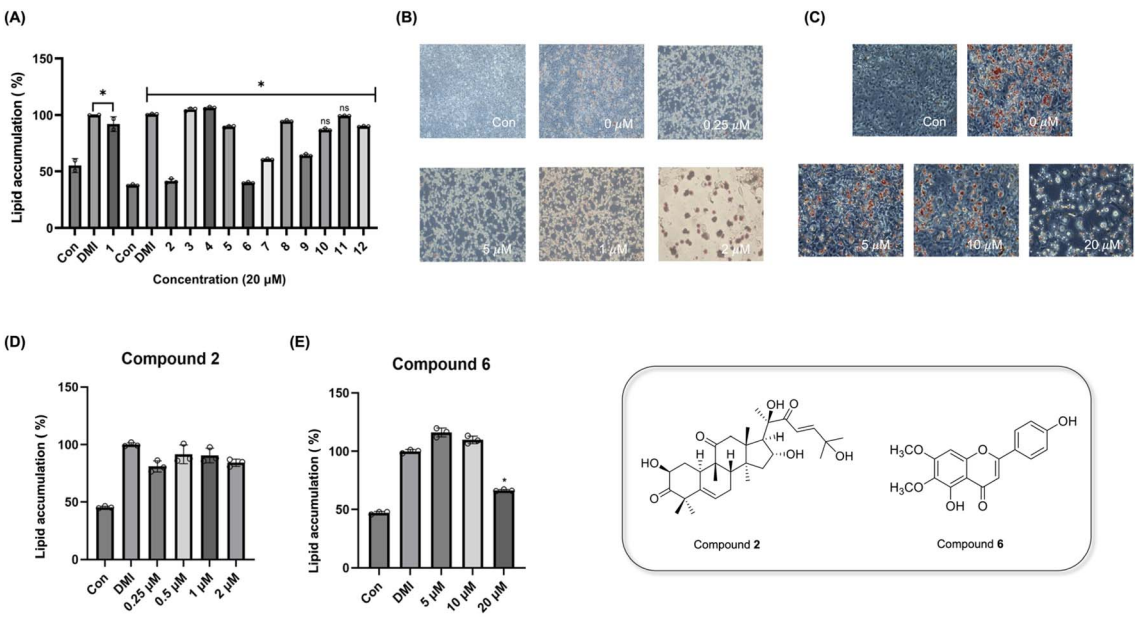

Fig. 4 Effects of compounds **1–12** on lipid accumulation in 3T3-L1 adipocytes. (A) Lipid accumulation under treatment with compound **1–12** at 20 μM. (B and C) Representative Oil Red O staining images compounds **2** and **6**, respectively. (D and E) Quantification of lipid accumulation of compounds **2** and **6**, respectively. Values are represented as mean ± standard deviation of three repeats. Statistical significance is indicated as **p* < 0.05 compared to DMI-treated.

evaluated. As shown in Fig. 4A, treatment with compounds **2** and **6** significantly reduced lipid accumulation by approximately 61% and 59%, respectively, compared to the positive control group, whereas compounds **1**, **3–5** and **7–12** did not show any significant inhibition. Notably, cirsimaritin (**6**) was identified as a major constituent of the *C. flagelliferum* extract, with an average content of 17.37 mg g^{-1} (Table S4), suggesting that **6** may be primarily responsible for the previously reported anti-obesity activity of *C. flagelliferum* extract.[18] Consequently, the dose-dependency of compounds **2** and **6** were further investigated.

Microscopic observations following Oil Red O staining demonstrated a notable reduction in both the size and number of red-stained lipid droplets in cells treated with either compound, relative to the control group. Based on preliminary results shown in Fig. 4A, the concentration of compound **2** was adjusted to 0.25–2 μM to mitigate cell detachment observed at higher concentrations, while no cytotoxicity was confirmed by the CCK-8 assay (Fig. S29). As shown in Fig. 4B and C, DMI-treated adipocytes exhibited abundant lipid droplets, whereas compound **2** and **6** markedly decreased the number and size of lipid droplets in a dose-dependent manner. Consistent with these results, the quantitative analysis of Oil Red O staining was performed. Despite being evaluated at a very low concentration (0.25–2 μM), compound **2** demonstrated inhibitory activity with an 8–19% reduction in lipid accumulation (Fig. 4B). Meanwhile, compound **6** showed a 34% reduction at 20 μM (Fig. 4C).

3.5. Inhibition of expression of adipogenic proteins in 3T3-L1 cells

To further evaluate the underlying mechanism of lipid inhibition, the expression levels of key adipogenic markers, C/EBP-α, PPAR-γ, perilipin-1, and FABP4, in 3T3-L1 cells were observed, following treatment of compounds **2** and **6**. Compound **2** resulted in a marked downregulation of all markers, especially PPAR-γ showing particularly strong suppression even at a very low concentration (0.25 μM) (Fig. 5A). In contrast, compound **6** showed a weaker and non-uniform inhibitory effects on adipogenic marker expression. C/EBP-α expression was reduced only at the highest concentration (20 μM), while the reduction in PPAR-γ was relatively modest in all tested concentrations. For downstream markers, FABP4 exhibited suppression at 5 μM, whereas perilipin-1 showed reduction at 10 μM (Fig. 5B). Interestingly, the increase in perilipin-1 level observed at a low concentration (5 μM) may reflect the dual role of perilipin-1 in lipid metabolism, functioning in both lipid droplet stabilization and lipolysis depending on its phosphorylation state.[39] These differential effects, particularly the weak inhibition of master regulators with relatively strong effects on downstream markers suggest that compound **6** may act through indirect modulation of adipogenic pathways, possibly *via* crosstalk between C/EBP-α and PPAR-γ.[40] Compounds **2** and **6** represent triterpenoids and flavonoids scaffolds, respectively, both of which have been implicated in the regulation of adipogenesis. Flavonoids, including apigenin, genistein and kaempferol, exhibit anti-obesity activity through the modulation of PPAR-γ,[41] with compound **6** demonstrating similar effects. In parallel, cucurbitacins B and I suppress PPAR-γ and C/EBP-α *via* STAT3-mediated pathways,[42] indicating that compound **2** may function through similar mechanisms.

While the anti-diabetic properties of compound **6** (ref. 43) and the anti-cancer/anti-inflammatory effects of compound **2** (ref. 44 and 45) are well-documented, this study is the first to establish that both compounds also possess anti-obesity activity *via* the modulation of adipogenic pathways. Collectively, these results indicate that *C. flagelliferum* produces structurally distinct anti-obesity compounds, providing a complementary multitarget therapeutic strategy for obesity.

3.6. Molecular docking

Based on the above results, compounds **2** and **6** significantly suppressed lipid accumulation and reduced the expression of

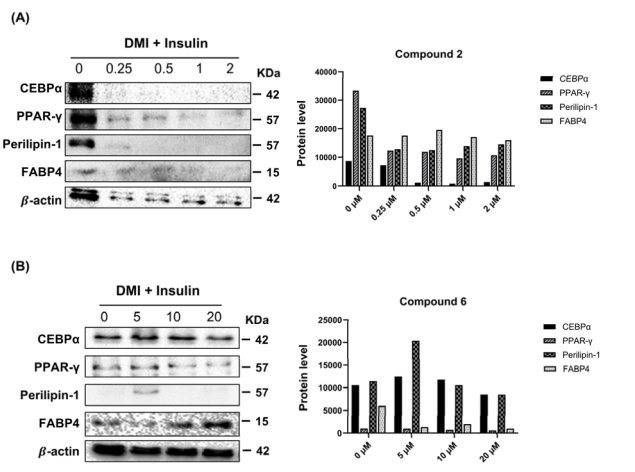

Fig. 5 Effects of compounds **2** and **6** on adipogenic marker protein expression in 3T3-L1 adipocytes. (A and B) Western blot analysis of adipogenic markers (C/EBPα, PPAR-γ, perilipin-1 and FABP4) in 3T3-L1 adipocytes treated with compounds **2** and **6**, respectively.

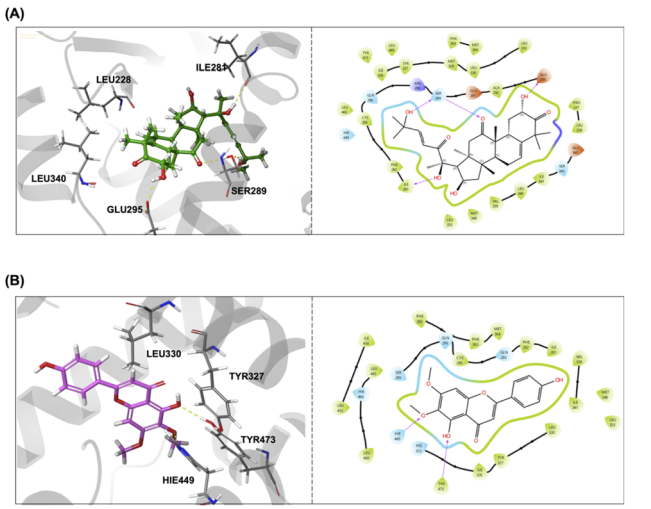

Fig. 6 Molecular docking analysis of compounds **2** and **6** with PPAR-γ (PDB ID: 3E00). (A and B) 3D and 2D interactions of compounds **2** and **6**, respectively.

key adipogenic markers. Since PPAR-γ functions as a master transcriptional regulator of adipogenesis[46] and its downstream target genes were markedly downregulated by compounds **2** and **6**, we sought to investigate whether compounds **2** and **6** interact with PPAR-γ. Therefore, molecular docking analysis was performed to predict the binding modes and affinities of compounds **2** and **6** with PPAR-γ. The results revealed that compounds **2** (−85.03 kcal mol^{-1}) and **6** (−80.94 kcal mol^{-1}) showed stronger binding affinities than GW9662 (−76.08 kcal mol^{-1}), a crystal ligand of 3E00. Particularly, compound **2** possesses a bulky steroidal scaffold that forms extensive van der Waals interactions with hydrophobic residues of PPAR-γ. In addition, it engages in hydrogen bonding with polar and charged residues such as Glu295, Ser289 and Ile281, thereby effectively occupying the binding pocket of PPAR-γ (Fig. 6A). Compound **6** adopts a planar polyphenolic scaffold and anchors to the binding pocket primarily through hydrogen bonding interactions with His449 and Tyr473. The binding is further stabilized by hydrophobic contacts with surrounding residues including His323, Ile326, Tyr327, and Leu330 (Fig. 6B). Therefore, based on the results of the molecular docking, MD simulations were performed to evaluate the dynamic behavior of PPAR-γ in complex with compounds **2** and **6** under simulated physiological conditions.

3.7. Structural stability of protein–ligand complexes

The overall structural stability of PPAR-γ complexes with compounds **2** and **6** was examined through a 500 ns MD simulation. The protein root mean square deviation (RMSD) of compound **2** complex remained relatively stable within the 4.5–6.0 Å range during the initial 200 ns of the simulation. However, following 220–250 ns, the protein RMSD exhibited a progressive increase, reaching a maximum of approximately 9–10 Å, suggesting significant structural rearrangement (Fig. 7A). Notably, despite this pronounced protein-level conformational change, the ligand RMSD remained consistently within the 2.5–3.5 Å range throughout the trajectory (Fig. 7B), indicating that the ligand maintained a stable binding pose within the binding pocket,[47] suggesting that the binding of compound **2** is resilient to global protein conformational fluctuations. In case of compound **6**–PPAR-γ complex, the protein RMSD exhibited an initial increase during the equilibration phase as the system adapted to the solvent environment, subsequently stabilizing at an average of approximately 4.4 Å (Fig. 7A). A transient elevation in RMSD was observed at approximately 150 ns; however, this fluctuation remained within the range of 1–3 Å, indicative of normal structural dynamics (Fig. 7A). Beyond 180 ns, the RMSD returned to baseline levels, demonstrating that the complex maintained a stable conformation throughout the simulation trajectory.

Consistently, ligand root mean square fluctuation (RMSF) analysis further investigates the fluctuations of individual ligand atoms around their average positions and provides insight into ligand flexibility and its entropic contribution to binding.[48] Compound **2** exhibited an average ligand RMSF of approximately 1.38 Å, whereas compound **6** showed an average

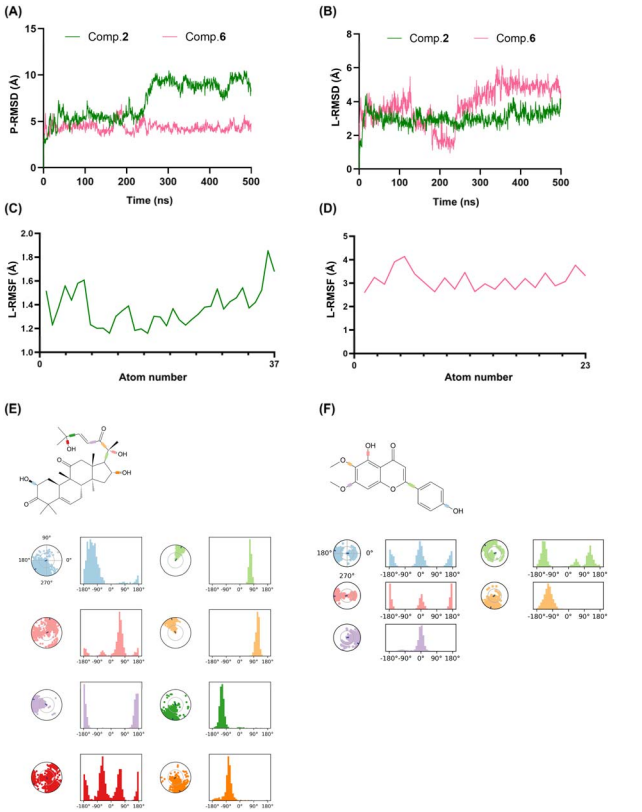

Fig. 7 Stability and conformational dynamics of the protein–ligand complex during the 500 ns simulation. (A) Protein RMSD of PPAR-γ complexes with compounds **2** and **6**. (B) Ligand RMSD of compounds **2** and **6**. (C and D) Ligand RMSF of compounds **2** and **6**, respectively. (E and F) Torsional distribution profiles of compounds **2** and **6**, respectively.

RMSF of approximately 3.13 Å (Fig. 7C and D). Both compounds maintained comparatively stable binding conformations throughout the simulation, with individual ligand atoms displaying acceptably low fluctuations consistent with tight binding to the PPAR-γ pocket.

Therefore, torsion profile analysis was performed to examine whether internal flexibility of the ligand contributed to the observed protein structural changes. The ligand torsion describes the conformational evolution of rotatable bonds in each ligand throughout the simulation trajectory. For compound **2**, the hydroxyl groups attached to the steroidal scaffold as well as the terminal hydroxyl group on the side chain exhibited considerable rotational flexibility, allowing the ligand to explore a broad torsional space (Fig. 7E). In contrast, compound **6** maintained more restricted torsional states, resulting in a narrower conformational distribution (Fig. 7F). This increased conformational flexibility of compound **2** likely promotes continuous ligand rearrangement within the binding pocket and may contribute to the increase in protein RMSD observed after the 200 ns.

3.8. Protein–ligand interactions

Protein–ligand interaction analysis was conducted to elucidate how each ligand maintains stable binding within the PPAR-γ

pocket. Throughout the simulation, although both compounds interacted with the common key residue Leu340, the residues contributing to the binding of both compounds differed over the course of the simulation, indicating distinct interaction patterns for compounds **2** and **6**. The top-5 residues interacting with compound **2** were identified as Leu228 (94.91%), Leu340 (75.72%), Gln286 (65.83%), Cys285 (58.54%) and Ser342 (58.54%) (Fig. 8A). Throughout the simulation, Leu228, Cys285, Leu340, and Ser342 maintained persistent interactions. In contrast, interaction with Gln286 was observed during the early stage of the simulation, exhibited a transient loss of interaction between approximately 43 and 126 ns, and subsequently re-established stable interactions for the remainder of the trajectory (Fig. 8B). For compound **6**, the major interacting residues were Leu340 (58.74%), Tyr327 (58.04%), Leu330 (42.06%), Tyr473 (39.76%), and His449 (34.37%) (Fig. 8C). Tyr327 and Leu330 maintained persistent interactions throughout the entire simulation. In contrast, Leu340 exhibited stable interactions until 350 ns, after which the interaction was lost. His449 showed strong interactions during the early phase of the simulation up to 246 ns, followed by a loss of contact until 350 ns and subsequent intermittent interactions. Tyr473 interacted with the ligand only during the initial 178 ns (Fig. 8D).

3.9. Overall properties of the ligand

Additionally, properties of the ligand, such as RMSD, radius of gyration (rGyr), intramolecular hydrogen bonds (intraHBs), molecular surface area (MolSA), solvent accessible surface area (SASA) and polar surface area (PSA), are shown in Fig. 9. Ligand RMSD analysis revealed that compound **2** exhibited fluctuations ranging from approximately 0.5 to 1.2 Å, while compound **6** displayed more restricted fluctuations within 0.25–0.75 Å. The broader RMSD range observed for compound **2** suggests that this compound undergoes more frequent conformational rearrangements within the binding pocket, whereas compound **6** undergoes more stable binding mode.

The rGyr values of the compounds **2** and **6**, which determine the compactness of the ligand, revealed distinct conformational behaviors.[49] Compound **6** remained compact with stable values of 4.3–4.5 Å (Fig. 9B), while compound **2** showed larger fluctuations ranging from 4.8 to 5.3 Å (Fig. 9A). A lower rGyr value signifies a stiffer structure, while a higher value indicates greater mobility within the complexes. These results indicate that compound **2** adopted a more extended and flexible structure, while compound **6** maintained a more compact and stable conformation within the binding pocket. IntraHBs formed within the ligand reflect the internal structural stability of the compound.[50] For compound **6**, intraHBs were frequently formed throughout the simulation, emphasizing their significance in maintaining a stable binding pose within the protein binding pocket (Fig. 9B). In contrast, compound **2** exhibited intraHBs only during the initial ~50 ns of the simulation, which were subsequently lost, indicating a lack of internal structural constraints to stabilize the ligand conformation (Fig. 9A).

To comprehensively understand ligand conformational stability and structural dynamics throughout the simulation, MolSA and SASA were first analyzed. MolSA represents the total surface of the ligand, equivalent to van der Waals surface area. Compound **6** maintained a relatively narrow MolSA range of 282–292 $Å^2$ (Fig. 9B), while compound **2** displayed a greater variability at approximately 432–447 $Å^2$ (Fig. 9A), reflecting its bulkier steroidal structure and more dynamic conformational rearrangements within the pocket. SASA, which reflects the ligand surface area accessible to solvent molecules, further highlighted differences in pocket occupancy between the two compounds. Compound **2** showed an early increase at 40–120

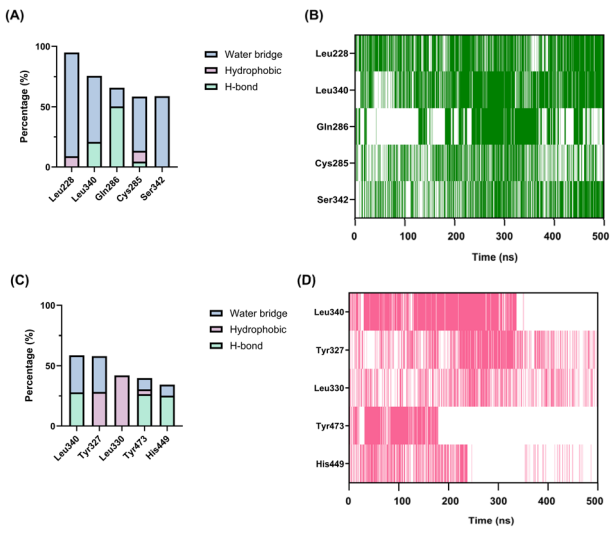

Fig. 8 Top-5 interacting residues and their interaction profiles during the 500 ns MD simulations. (A and B) Interaction frequencies and timelines of the top-5 interacting residues of compound **2** with PPAR-γ. (C and D) Interaction frequencies and timelines of the top-5 interacting residues of compound **6** with PPAR-γ.

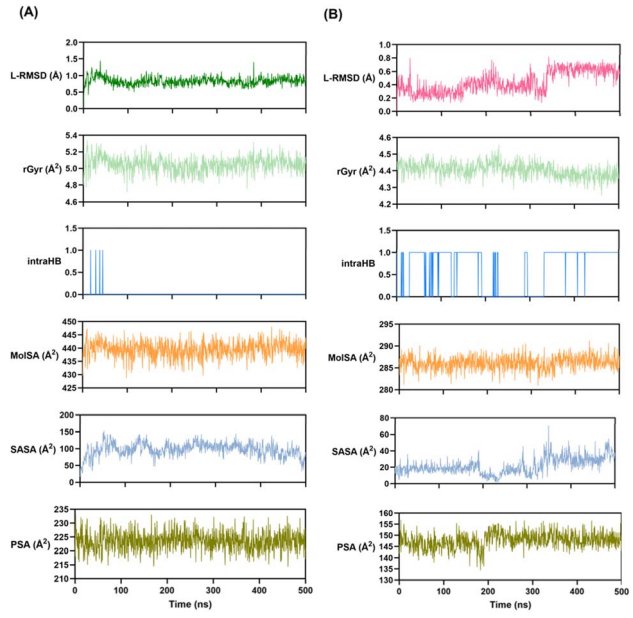

Fig. 9 (A and B) Overall ligand properties of compounds **2** and **6**, respectively.

Å^2, followed by stabilization at ~99 Å^2 (Fig. 9A). Compound **6** remained stable at approximately 19 Å^2 until around 191 ns, with minor fluctuations between 192–240 ns thereafter that quickly re-stabilized, indicating consistent pocket occupancy (Fig. 9B).[49]

Subsequently, PSA analysis was conducted to determine whether the conformational changes influenced the exposure of polar functional groups. Compound **2** fluctuated broadly between 216–230 Å^2 due to free rotation of hydroxyl groups on its scaffold and side chain (Fig. 9A). Compound **6** showed PSA variations of 144–152 Å^2 until 160 ns, 136–153 Å^2 between 160–200 ns, and then stabilized thereafter, indicating a more constrained polar group orientation (Fig. 9B).

The overall MD results indicate that compounds **2** and **6** exhibit distinct interaction modes with PPAR-γ. Compound **2** exhibited relatively high internal torsional flexibility, resulting in continuous conformational rearrangement within the binding pocket and high protein RMSD. Despite this dynamic behavior, the ligand maintained persistent interactions with key residues, suggesting a binding mode characterized by adaptive ligand conformation with stable residue anchoring. In contrast, compound **6** adopted a more rigid structure with restricted torsional freedom, stabilized by intraHBs. Although several residue interactions showed temporal variability (His449, Tyr473 and Leu340), the ligand itself maintained a stable binding pose with consistently low RMSD values, indicating that compound **6** archives binding stability through its inherent structural rigidity.

4 Conclusions

In this study, a comprehensive phytochemical investigation of the unexplored Korean native plant *Chrysosplenium flagelliferum* was conducted, leading to the isolation of twelve compounds (**1–12**), including a newly identified triterpene glycoside (**1**). All isolated compounds were evaluated for their anti-obesity potential. Among these, compounds **2** and **6** exhibited significant anti-lipid accumulation effects in 3T3-L1 adipocytes. Western blot analysis revealed that both compounds modulated the expression of the adipogenic master regulators C/EBPα and PPAR-γ, indicating suppression of the adipogenic program. To elucidate the molecular basis of PPAR-γ modulation, molecular docking and MD simulation were further performed, highlighting that compounds **2** and **6** interact with PPAR-γ through different binding mechanisms. Compound **6** maintained a stable and compact binding pose. In contrast, although compound **2** showed favorable docking scores, its greater conformational dynamics due to structural flexibility, resulted in dynamic binding behavior. These findings suggest that structural optimization stabilizes its binding pose for enhanced drug-likeness. Overall, this study demonstrates the anti-obesity activity of *C. flagelliferum*-derived compounds for the first time, highlighting their potential as promising therapeutics candidates. However, as this research is based solely on *in vitro* experiments, further validation using high-fat diet-induced obese mouse models is required to confirm the anti-obesity efficacy and safety of *C. flagelliferum*-derived compounds under physiological conditions. This research provides foundational understanding that could accelerate the development of natural product-based anti-obesity therapeutics, emphasizing the need for future animal studies and yield optimization through improved isolation or synthetic approaches.

Author contributions

Conceptualization – J. A. Kim, S. Lee; data curation – E. J. Heo, B. Jung; formal analysis – E. J. Heo, B. Jung, S. Kwon, M. Y. Choi, Y. S. Jang; investigation – E. J. Heo, B. Jung, S. Kwon, M. Y. Choi, Y. S. Jang; methodology – E. J. Heo, B. Jung, M. Y. Choi; resources – G. H. Park, J. A. Kim; validation – E. J. Heo, B. Jung, G. H. Park, K. H. Kim; visualization – E. J. Heo, B. Jung, M. Y. Choi; supervision – K. H. Kim, G. H. Park, J. A. Kim, S. Lee; writing – original draft – E. J. Heo, B. Jung, S. Kwon, M. Y. Choi; writing – review & editing – J. A. Kim, S. Lee; funding acquisition – J. A. Kim, S. Lee; project administration – S. Lee.

Conflicts of interest

The authors declare that they have no conflict of interest.

Data availability

All data supporting the findings of this study are available within the article and its supplementary information (SI). ^{1}H^{13}C**12** and **6**Supplementary information: copies of the ^{1}H-NMR, ^{13}C-NMR, 2D NMR (HSQC, HMBC, COSY and ROESY), physical data (MS and UV spectra), DP4+ computational analysis for stereochemical assignment of compound **1**, quantitative analysis, and cell cytotoxicity data for compound **2** and **6**. See DOI: https://doi.org/10.1039/d6ra00782a.

Acknowledgements

This work was supported by the National Research Foundation of Korea (NRF) grant funded by the Korea government (MSIT) (No. RS-2023-00212670) and by Global – Learning & Academic research institution for Master's·PhD students, and Postdocs (G-LAMP) Program of the NRF grant funded by the Ministry of Education (No. RS-2025-25442355). This work was also supported by the Forest Medicinal Resources Research Center of the National Institute of Forest Science (NIFoS) (No. FP0802-2023-01-2025).

References

1 H. Hara, *J. Fac. Sci., Imp. Univ. Tokyo, Sect. 3*, 1957, **7**, 1–90.
2 L.-F. Fu, R. Liao, D.-Q. Lan, F. Wen and H. Liu, *PhytoKeys*, 2020, **159**, 127.
3 Y.-I. Kim, J.-S. Shin, S. Lee, J.-H. Chen, S. Choi, J. H. Park and Y.-D. Kim, *PhytoKeys*, 2019, **135**, 39.
4 B. Forbes and W. B. Hemsley, *Enumeration of all the plants known from China proper, Formosa, Hainan, the Corea, the Luchu Archipelago, and the island of Hongkong: Together with*

their distribution and synonymy, Linnean Society, 1888, vol. 23.
5 H.-J. Kim, H.-S. Jeong and S.-H. Kang, *Korean J. Plant Resour.*, 2013, **26**, 718–725.
6 J. Zhao, X. Qiu, Y. Zhao, R. Wu, P. Wei, C. Tao and L. Wan, *J. Ethnopharmacol.*, 2022, **290**, 115042.
7 B. A. Bohm and F. Collins, *Biochem. Syst. Ecol.*, 1979, **7**, 195–201.
8 M. A. Olszewska and J. Gudej, *J. Pharm. Biomed. Anal.*, 2009, **50**, 771–777.
9 H.-A. Choi, D.-E. Cheong, H.-D. Lim, W.-H. Kim, M.-H. Ham, M.-H. Oh, Y. Wu, H.-J. Shin and G.-J. Kim, *J. Microbiol. Biotechnol.*, 2017, **27**, 1242–1248.
10 M. Arisawa, T. Hatashita, Y. Numata, M. Tanaka and T. Sasaki, *Int. J. Pharmacogn.*, 1997, **35**, 141–143.
11 M. Arisawa, T. Hayashi, M. Shimizu, N. Morita, H. Bai, S. Kuze and Y. Ito, *J. Nat. Prod.*, 1991, **54**, 898–901.
12 M. Arisawa, M. Shimizu, Y. Satomi, A. Nishino, H. Nishino and A. Iwashima, *Phytother. Res.*, 1995, **9**, 222–224.
13 Y. Tsuchiya, M. Shimizu, Y. Hiyama, K. Itoh, Y. Hashimoto, M. Nakayama, T. Horie and N. Morita, *Chem. Pharm. Bull.*, 1985, **33**, 3881–3886.
14 B. Ahmad, E. P. Friar, M. S. Vohra, N. Khan, C. J. Serpell, M. D. Garrett, J. S. E. Loo, I. L. Fong and E. H. Wong, *Chem.-Biol. Interact.*, 2023, **379**, 110503.
15 J. Park, E. Lee and J.-O. Nam, *J. Appl. Biol. Chem.*, 2025, **68**, 204–211.
16 H. J. Lim and Y. G. Yoon, *J. Appl. Biol. Chem.*, 2023, **66**, 328–337.
17 J. S. Kim, S. G. Lee, K. Min, T. K. Kwon, H.-J. Kim and J.-O. Nam, *Biomed. Pharmacother.*, 2018, **103**, 135–139.
18 J. W. Choi, G. H. Park, H. J. Choi, J. W. Lee, H.-Y. Kwon, M. Y. Choi and J. B. Jeong, *Exp. Ther. Med.*, 2024, **28**, 315.
19 A. T. Aron, E. C. Gentry, K. L. McPhail, L.-F. Nothias, M. Nothias-Esposito, A. Bouslimani, D. Petras, J. M. Gauglitz, N. Sikora and F. Vargas, *Nat. Protoc.*, 2020, **15**, 1954–1991.
20 B. S. Lee, H. Kim, J. Baek, R. Ryoo, S. R. Lee and K. H. Kim, *Pharmaceutics*, 2024, **16**, 364.
21 C. S. Kim, J. Oh, L. Subedi, S. Y. Kim, S. U. Choi and K. R. Lee, *J. Nat. Prod.*, 2018, **81**, 1795–1802.
22 J. S. Yu, M. Park, C. Pang, L. Rashan, W. H. Jung and K. H. Kim, *J. Nat. Prod.*, 2020, **83**, 2261–2268.
23 S. G. Smith and J. M. Goodman, *J. Am. Chem. Soc.*, 2010, **132**, 12946–12959.
24 N. Grimblat, M. M. Zanardi and A. M. Sarotti, *J. Org. Chem.*, 2015, **80**, 12526–12534.
25 C. Seger, S. Sturm, E. Haslinger and H. Stuppner, *Monatsh. Chem.*, 2005, **136**, 1645–1649.
26 Y. Yamada, K. Hagiwara, K. Iguchi, S. Suzuki and H. Hsu, *Chem. Pharm. Bull.*, 1978, **26**, 3107–3112.
27 H. Jacobs, T. Singh, W. F. Reynolds and S. McLean, *J. Nat. Prod.*, 1990, **53**, 1600–1605.
28 Y. Yamada, K. Hagiwara, K. Iguchi and S. Suzuki, *Tetrahedron Lett.*, 1977, **18**, 2099–2102.
29 Y. Soon-Ho, K. Hyun Jung and L. Ik-Soo, *Arch. Pharmacal Res.*, 2003, **26**, 128–131.
30 N. Bai, K. He, Z. Zhou, C.-S. Lai, L. Zhang, Z. Quan, X. Shao, M.-H. Pan and C.-T. Ho, *Food Chem.*, 2010, **122**, 831–835.
31 P. Majumder and R. Sen, *Phytochemistry*, 1991, **30**, 2432–2434.
32 J. Gudej and P. Czapski, *Chem. Nat. Compd.*, 2009, **45**, 717–719.
33 D. Zhao, N. Wu, S. Zhang, P. Xi, X. Su, J. Lan and J. You, *Angew. Chem., Int. Ed.*, 2009, **48**, 8729–8732.
34 R. A. Olsen, L. Liu, N. Ghaderi, A. Johns, M. E. Hatcher and L. J. Mueller, *J. Am. Chem. Soc.*, 2003, **125**, 10125–10132.
35 W. A. Bubb, *Concepts Magn. Reson., Part A*, 2003, **19**, 1–19.
36 C. Chen, S. Qiang, L. Lou and W. Zhao, *J. Nat. Prod.*, 2009, **72**, 824–829.
37 X.-S. Li, Q.-L. Wang, Z.-P. Xu, M.-S. Liu, X.-Y. Liang, J.-C. Zheng, H.-Y. Deng, L. Liu, Y.-M. Huang and M.-X. Yang, *Phytochemistry*, 2024, **220**, 114033.
38 M. Wang, J. J. Carver, V. V. Phelan, L. M. Sanchez, N. Garg, Y. Peng, D. D. Nguyen, J. Watrous, C. A. Kapono and T. Luzzatto-Knaan, *Nat. Biotechnol.*, 2016, **34**, 828–837.
39 J. Bi, Y. Xiang, H. Chen, Z. Liu, S. Grönke, R. P. Kühnlein and X. Huang, *J. Cell Sci.*, 2012, **125**, 3568–3577.
40 Z. Wu, E. D. Rosen, R. Brun, S. Hauser, G. Adelmant, A. E. Troy, C. McKeon, G. J. Darlington and B. M. Spiegelman, *Mol. Cell*, 1999, **3**, 151–158.
41 A. K. d. S. Oliveira, A. M. de Oliveira e Silva, R. O. Pereira, A. S. Santos, E. V. Barbosa Junior, M. T. Bezerra, R. S. Barreto, L. J. Quintans-Junior and J. S. Quintans, *Crit. Rev. Food Sci. Nutr.*, 2022, **62**, 7827–7848.
42 C.-R. Seo, D. K. Yang, N.-J. Song, U. J. Yun, A.-R. Gwon, D.-G. Jo, J. Y. Cho, K. Yoon, J.-Y. Ahn and C. W. Nho, *Food Chem. Toxicol.*, 2014, **64**, 217–224.
43 A. Alqudah, R. Y. Athamneh, E. Qnais, O. Gammoh, M. Oqal, R. AbuDalo, H. A. Alshaikh, N. Al-Hashimi and M. Alqudah, *Int. J. Mol. Sci.*, 2023, **24**, 5749.
44 M. Sikander, B. B. Hafeez, S. Malik, A. Alsayari, F. T. Halaweish, M. M. Yallapu, S. C. Chauhan and M. Jaggi, *Sci. Rep.*, 2016, **6**, 36594.
45 Y. Song, N. Ding, T. Kanazawa, U. Yamashita and Y. Yoshida, *Int. Immunopharmacol.*, 2013, **17**, 1044–1050.
46 E. D. Rosen and O. A. MacDougald, *Nat. Rev. Mol. Cell Biol.*, 2006, **7**, 885–896.
47 S. Patel, A. D. Mackerell Jr and C. L. Brooks III, *J. Comput. Chem.*, 2004, **25**, 1504–1514.
48 N. B. Bhat, S. Das, B. V. Sridevi, S. Nayaka, S. R. Birangal, G. G. Shenoy and A. Joseph, *J. Biomol. Struct. Dyn.*, 2023, **41**, 11484–11497.
49 A. Samad, M. A. Huq and M. S. Rahman, *Sci. Rep.*, 2022, **12**, 1539.
50 G. Vogt, S. Woell and P. Argos, *J. Mol. Biol.*, 1997, **269**, 631–643.